Enhancing aromatics extraction by double salt ionic liquids: rational screening-validation and mechanistic insights

Kunchi Xie[a], Jiahui Chen[a], Ruizhuang Wang[a], Jie Cheng[a], Hongye Cheng[a], Zhiwen Qi[a,*], Kake Zhu[a] and Zhen Song[a,b*]

[a]*State Key laboratory of Chemical Engineering, School of Chemical Engineering, East China University of Science and Technology, 130 Meilong Road, Shanghai 200237, China*

[b]*Engineering Research·Center of Resource Utilization of Carbon-containing Waste with·Carbon Neutrality (Ministry of Education), East China University of Science and Technology, 130 Meilong Road, Shanghai 200237, China*

Corresponding authors: *zwqi@ecust.edu.cn*; *songz@ecust.edu.cn*

Abstract:

Despite offering remarkable advantages as solvents, double salt ionic liquids (DSILs) have been scarcely studied for extractive dearomatization from hydrocarbons as well as many other applications, thus urging a theoretical guidance method. In this work, a systematic framework combining the rational screening-validation and mechanistic analysis is proposed for tailoring DSILs for the *o*-xylene/*n*-octane separation. From an initial pool of commercially available ionic liquids (ILs), key thermodynamic properties of paired DSILs are predicted by COSMO-RS while their important physical properties are estimated from those of corresponding parent ILs (retrieved from experimental database or predicted by a deep learning model). Promising DSILs are tested by liquid-liquid equilibrium experiments, wherein the ion ratio-effect is also evaluated. The mechanism underlying the tunability of DSIL thermodynamic properties is disclosed by means of quantum chemistry calculation and molecular dynamics simulation. This work can be a valuable reference for guiding the design of DSILs for diverse applications.

KEYWORDS: double salt ionic liquids, aromatics extraction, solvent screening-validation, LLE experiment, mechanistic analysis

1. INTRODUCTION

In the petrochemical industry, selective separation of aromatics from hydrocarbon mixtures is of great significance as it is not only relevant for producing fuel oils meeting specific standards but also necessary for obtaining high-purity aromatics and hydrocarbons as feedstocks for downstream processes. Depending on the aromatic content in the mixture, different separation processes should be utilized, among which liquid-liquid extraction is typically employed to extract aromatics from hydrocarbon streams with concentrations ranging from 20 to 65wt%.[1] The main organic solvents reported in the literature for such liquid−liquid extraction processes are sulfolane, *N*-methylpyrrolidone, dimethyl sulfoxide, *N*-formylmorpholine, among others.[2,3] Nevertheless, these organic solvents generally possess unfavorable physical properties such as high volatility and toxicity, which potentially impede the subsequent solvent regeneration and lead to expensive operational cost as well as environmental concerns. Hence, exploring alternative extractants with superior characteristics are highly desirable.

Ionic liquids (ILs) have been extensively studied as an alternative solvent option due to their negligible volatility, wide liquidus range, designable character, etc.[4–12] However, given the vast chemical space of potential IL candidates, the experimental trial-and-error approach is clearly costly and inefficient for large-scale IL selection. Therefore, several works have proposed computational screening and design methods to guide the identification of promising IL solvents toward various processes.[13–16]

Nevertheless, in many cases, it is still a great challenge to select a satisfying IL as very few ILs can meet different property constraints simultaneously. For example, during the IL screening for desulfurization, Song et al.[17] uncovered that only 831 out of 36,260 IL candidates meet the thermodynamic property requirements; if physical property constraints of melting point and viscosity are further considered, only 15 IL candidates are survived. It could be anticipated that if more constraints (e.g., low cost and potential availability) are imposed in the screening, fewer or even no promising ILs will be retained.

Eutectic solvents (ESs), in some cases also coined as deep eutectic solvents (DESs) have recently emerged as another promising solvent option.[18–25] Bearing similar physicochemical properties to ILs, ESs have been widely regarded as "IL analogues". More attractively, ESs can be prepared with 100% atom economy by simply mixing hydrogen bond donor (HBD) and hydrogen bond acceptor (HBA), for which many potential HBA: HBD combinations as well as their mixing ratio offer a more flexible property tunability as opposed to ILs. However, differing from the strong electrostatic interaction in ILs, the hydrogen bond formed between HBA and HBD is relatively weak, which may lead to poor compositional stability of ESs in use. In other words, there may exist intractable problems in the subsequent regeneration and reuse of ESs in practical applications. For example, Sun et al.[23] experimentally studied the extraction of benzene/cyclohexane mixtures by $[N_{4444}]$Br: sulfolane (1:3 and 1:7), which both show stronger affinity toward benzene against cyclohexane; Cheng et al.[24] screened the $[N_{4444}]$Br: DMF (1:3) for extractive desulfurization after evaluating the extractive potential of 49 ESs by the COSMO-RS model. Despite the comparable and even superior extraction performance of these ESs over commercial solvents in these cases, the mildly polar HBDs are susceptible to be partly distributed in the hydrocarbon phase.

Moving beyond classical two-ion ILs (i.e., one cation and one anion) and ESs, double salt ionic liquids (DSILs) that consist of more than one cation and/or anion have also attracted wide attention as a unique, promising solvent option.[26–31] Since the most straightforward way to obtain DSILs is to mix different ILs (in the following, all "ILs" refers to two-ion ILs without clarification) together, they are also directly regarded as "IL mixtures" in many cases. Regardless of the different terminologies, this type of solvents could well combine the merits of ILs and ESs to a large extent. When compared to ILs, DSILs greatly extend the solvent selection space and provides an easier way to tune solvent properties. To be specific, (1) the number of DSILs could be many orders of magnitude larger by simply mixing different ILs, and even if the commercially or experimentally synthesized ILs are considered only, a broad scope of DSILs would still be provided; (2) the properties of DSILs could be readily tuned in a wide range by simply changing the IL parents and/or the corresponding ratios, whereas the properties of ILs usually have to be altered by changing the alkyl chain length and/or functionalization (resulting in complex synthesis and purification processes). Note that, the flexible property tunability of DSILs is similar to that of ESs. Meanwhile, DSILs featuring internal electrostatic interaction could secure a higher compositional stability as opposed to ESs when applied in mixture systems, which is highly favorable from the solvent regeneration and reuse point of view. For these reasons, DSILs open up new opportunities for the selection of appropriate solvents for various chemical processes, including the liquid-liquid extraction.

Larriba et al.[27] performed the dearomatization of a pyrolysis gasoline model using the {[C_2MIm][TCM] + [C_2MPy][NTf_2]} with different molar ratios, which allow a better trade-off between the aromatic distribution coefficient and selectivity than the individual ILs. Lee et al.[28] investigated the solubility of paracetamol in DSILs that could

be formed by 82 cations and 32 anions via the COSMO-SAC model, emphasizing the classification and σ-profile-based analysis of ideal or non-ideal behaviors of DSILs as opposed to the parent ILs. Song et al.[29] applied the COSMO-RS model for evaluating the effect of introducing double cations and/or anions and different ion ratios on the extractive potential of DSILs for thiophene/n-octane separation, which further guided the screening of hypothetical DSILs from all possible combinations of 20 cations and 25 anions. Despite of these works that have demonstrated the great potential of DSILs as solvent, it should be noted that DSILs are much less scarcely studied as compared to ILs and ESs in the literature. Moreover, most available studies on DSILs are limited to either experimental measurement or model-based estimation of properties of DSILs toward a given application. A comprehensive study ranging from the rational task-specific DSIL selection to the deep mechanistic analysis is still lacking.

Considering all the above aspects, this work systematically investigates DSILs for the aromatics extraction from hydrocarbons (with *o*-xylene/*n*-octane as a model mixture) by combining a rational screening-validation of practical DSILs and a thorough microscopic mechanism exploration. A database of commercially available ILs is first collected as an initial pool of parent ILs for pairing practical DSILs. The extractive potential of thus obtained DSILs are then evaluated by combining thermodynamic property calculation by COSMO-RS and physical property assessment by empirical estimation from those of the parent ILs (for which missing properties are predicted by a very recently reported deep learning model[32]). DSILs satisfying both thermodynamic and physical property criteria are further studied by liquid-liquid equilibrium (LLE) experiment, wherein different DSILs and the effect of different ion ratios are validated and compared with the ILs that are screened in a similar procedure. The enhanced extraction performance of DSILs is finally unveiled at the microscopic scale by

quantum chemistry calculation and molecular dynamics simulation.

2. METHOD

The research framework proposed in this work is shown in Figure 1, which consists of four main steps. First, instead of assuming hypothetical DSILs from random combinations of cations and anions, a database of commercially available ILs is collected from the suppliers of Aladdin, Maclin, Lanzhou Institute of Chemical Physics to secure the accessibility of practical DSILs in the subsequent steps. The second step is the thermodynamic and physical property-based screening. Specifically, the COSMO-RS model is applied for the calculation of infinite dilution capacity (C^{∞}) and selectivity (S^{∞}) of DSILs, while empirical estimations are made for the melting points (T_m) and viscosities (η) of DSILs based on the counterparts of the parent ILs (experimental data are referred if available, and otherwise model predictions by a very recently reported deep learning model are used). Constraints are imposed on the T_m and η for screening DSILs suitable as extractants, and sulfolane is taken as a reference solvent in this case for screening DSILs with satisfactory extractive potential. In the third step, liquid-liquid equilibrium (LLE) experiments are systematically performed to test the above screened DSILs and study the effect of different ion ratios. The fourth step is the microscopic mechanism analyses by combining quantum chemistry calculation and molecular dynamics simulation, wherein the intermolecular interaction energy, independent gradient model (IGM), radial distribution function (RDF), and spatial distribution function (SDF) are computed.

In the following, more details regarding the thermodynamic and physical property-based screening, experimental validation, and mechanism analyses involved in the proposed research framework are provided.

2.1 Thermodynamic property screening

To select promising DSIL extractants, it is of primary significance to evaluate their extractive potential from thermodynamic point of view. To this end, the COSMO-RS model is utilized to predict the infinite dilution capacity and selectivity (i.e., C^{∞} and S^{∞}) of different DSILs for the *o*-xylene/*n*-octane separation as follows:

$$C^{\infty}=1/\gamma^{\infty}_{o\text{-xylene}} \tag{1}$$

$$S^{\infty}=\gamma^{\infty}_{n\text{-octane}}/\gamma^{\infty}_{o\text{-xylene}} \tag{2}$$

where $\gamma^{\infty}_{o\text{-xylene}}$ and $\gamma^{\infty}_{n\text{-octane}}$ represent the infinite dilution activity coefficients of *o*-xylene and *n*-octane in DSILs, respectively. The C^{∞} and S^{∞} could be rapid and simple indicators of the extractive potential of DSILs for separating *o*-xylene from *n*-octane. The COSMO-RS model has been discussed detailedly in previous literatures on its application in calculating various thermodynamic properties.[33] It is widely recognized to be able to provide qualitatively reliable and quantitatively acceptable predictions in most cases for the thermodynamic properties of IL-involved systems,[16,34–37] and therefore is also potentially suitable for estimating the separation performance of DSILs.[28,29,38] In this work, all COSMO-RS calculations are performed using the COSMOthermX software package (Version 22.0) at the BP86/TZVP level under the BP_TZVP_22.ctd parameterization. The COSMO files for anions/cations of ILs, *n*-octane, and *o*-xylene are directly taken from COSMObase (Version 22.0, COSMOlogic GmbH).

It is worth noting that in COSMO-RS calculation, ILs including DSILs are treated as electrically neutral mixtures consisting of separate cations and anions, whereas in experiments they are treated as one compound. Therefore, as detailed in the COSMOthermX manual (Version C3.0, Release 16.01), the computed thermodynamic

properties that rely on the definition of mole fraction (such as the infinite dilution activity coefficients) must be converted to ensure consistency with the reference standard used in experiments. As the C^{∞} and S^{∞} are essentially derived from the infinite dilution activity coefficient, all the calculated results by COSMO-RS has been converted accordingly in this work.

2.2 Physical property screening

Apart from the thermodynamically extractive potential, the T_m and η of solvent are also important factors that need to be taken into account for extraction processes. As the study of DSILs is currently still scarce, there is no available model that can be applied to estimate T_m and η of them directly. However, according to previous reports,[30,39] DSIL in many cases possesses a lower T_m than its IL parents, presenting as an ES-like system. For this reason, the T_m of at least one parent IL is constrained to be below 298.15 K. As for the viscosity, which is an out-of-equilibrium and non-molar quantity, the Grunberg-Nissan mixing rule was suggested to be a suitable mixing law for DSILs by showing a high accuracy in predicting η of the imidazolium- and pyridinium-based IL "mixtures" from those of their parent ILs.[40,41] Therefore, η of DSILs are assessed from those of their IL parents by applying this mixing rule:[42]

$$log_{10}(\eta) = \sum_{i=1}^{2} x_i \log_{10}(\eta_i) \quad (3)$$

where x_i and η_i refer to the molar fraction and viscosity of parent IL, η denotes the predicted viscosity of DSIL. Following this, the upper bound of the η of DSILs is set to be 100 mPa·s.

In this work, the T_m and η of the parent ILs of DSILs are first collected from ILThermo (version 2.0).[43] Experimental data available will be directly used, otherwise estimations will be made by applying a recently reported deep learning model.[32] The

applied deep learning method is a novel two-stage ILTransR architecture combining pre-training by Transformer and fine-tuning by convolutional neural network (CNN), which employs large-scale unlabeled data for generalizing IL property prediction from limited labeled data. Through case studies covering eleven IL properties (including the two properties considered here), it was demonstrated that the ILTransR method surpasses various state-of-the-art models in the literature. Specifically, for the T_m and η of ILs, the ILTransR method gives a much lower mean absolute error (11.15 for T in K, 0.35 for lnη in mPa·s) as opposed to the reference models in the literature. More details about the two-stage ILTransR architecture for IL property prediction can be referred to Chen et al.[32]

It should be mentioned that the estimation of T_m and η of DSILs based on those of their parent ILs may lead to some deviations in certain cases. In the long term, further experimental studies along with the development of reliable models on the fundamental physical properties of DSILs are highly desirable.

2.3 Experimental validation

For promising DSIL candidates identified after thermodynamic and physical property screening, it is important to verify the practical extraction performance through experiments. Therefore, for the separation of *o*-xylene/*n*-octane model mixture, LLE experiments of {DSILs + *o*-xylene + *n*-octane} are carried out. The IL parents used for preparing DSILs are purchased from Adamas-beta and Macklin with purity above 98.0 wt%, and treated by rotary evaporation at 10 kPa and 353 K for 24 hr to remove possible volatile impurities and traces of water before use. *o*-Xylene and *n*-octane are supplied by Adamas-beta with purity above 99.0 wt%, and used as received without further purification.

Before the LLE experiment, the DSILs are prepared by mixing two ILs at a desired

molar ratio at atmospheric pressure and 298.15 K, wherein the mass of each IL is weighed by a Sartorius BSA224S-CW balance (Germany) with a precision of ±0.0001 g. After stirring at 500 rpm for 1 hr and settling for 1 hr, visual inspection is taken to check whether a homogenous DSIL is obtained. In a typical LLE, the DSIL, *o*-xylene, and *n*-octane are added successively into a 10 ml screw-capped vial, wherein their masses are gravimetrically measured. After tightly sealed, the mixture is stirred at 500 rpm for 8 hr and then settles for another 8 hr to ensure complete thermodynamic equilibrium. The temperature of the liquid mixture is controlled by an oil bath (Huber Ministat 230, Germany) with a temperature fluctuation of ±0.1 K. After settling, samples of the upper (raffinate) and lower (extract) layers are carefully withdrawn using syringes and analyzed by a gas chromatograph (Agilent 7890 GC) equipped with a flame ionization detector (FID) and an HP-FFAP (30 m, 0.32 mm, 0.25 mm) capillary column.

The mass fraction of *o*-xylene and *n*-octane in both phases is determined by using undecane as internal standard. The GC analyses are carried out under the heating procedure of maintaining the initial temperature of 353.15 K for 2 min, ramping 60 K/min to 503.15 K, and settling for 5 min. The high-purity nitrogen with 99.999 wt% is applied as the carrier gas with a flow rate of 20 ml/min. Each sample is analyzed three times and each experiment is repeated twice. The distribution coefficient (β) and selectivity (S) of DSILs at the specific *o*-xylene/*n*-octane mixture composition are calculated as:

$$\beta = m^{E}_{o\text{-xylene}} / m^{R}_{o\text{-xylene}} \tag{4}$$

$$S = \frac{m^{E}_{o\text{-xylene}}}{m^{R}_{o\text{-xylene}}} \Big/ \frac{m^{E}_{n\text{-octane}}}{m^{E}_{n\text{-octane}}} \tag{5}$$

where the $m^{E}_{o\text{-xylene}}$ and $m^{R}_{o\text{-xylene}}$ refer to the mass fraction of *o*-xylene in the extract and

raffinate phases, respectively.

2.4 Quantum chemistry calculation

The intermolecular interaction and microstructure are analyzed by density functional theory (DFT) method using the Gaussian 09 (version E.01).[44,45] The geometry of each compound is optimized at the B3LYP/6-31+G (d, p) theoretical level,[46] along with DFT-D3(BJ) dispersion corrections.[47] As the calculation of {DSIL + *o*-xylene/*n*-octane} interaction energies at different molar ratios of parent ILs is difficult, geometric structures between each parent IL and *o*-xylene/*n*-octane are optimized, followed by the interaction energy calculation as a reference for the DSILs-involved systems. To be specific, different {IL + *o*-xylene/*n*-octane} combination modes are used to determine the most stable structures for structure optimization. Meanwhile, the intermolecular interaction energy (E_{inter}) is calculated by:[48]

$$E_{inter}=E_{A+B}-E_A-E_B+E_{BSSE} \quad (6)$$

where E_{A+B}, E_A, E_B and E_{BSSE} are the energies of A with B, a single A, a single B, and the basis set superposition error, respectively. Besides, the intermolecular interaction between DSIL and *o*-xylene/*n*-octane have also been analyzed by the IGM approach using the Multiwfn 3.8 program,[49,50] which could be visually shown by Visual Molecular Dynamics software (version 1.9.3).[51] By such IGM analysis, an intuitive and comprehensive depiction of the locations and properties of intermolecular interactions can be provided.

2.5 Molecular dynamics simulation

The widely-used GROMACS code has been utilized for the implementation of molecular dynamics simulation and subsequent theoretical analyses for the extraction systems involved in this work.[52] The geometries of each ion and molecular compound

have been optimized using the Gaussian 09 software at the B3LYP/6-31+G (d, p) theoretical level, followed by the derivation of partial atomic charges through the RESP method.[53] The force field parameters of anion, cation, *n*-octane, and *o*-xylene applied here are all obtained from the GAFF force field.[54] Energy minimization is performed for each system using the steepest descent method in advance. Then, heating and quenching steps are carried out as follows: (i) heating up to 700 K, (ii) simulating in isothermal-isobaric (NPT) ensemble at 700 K and 1 bar for 1 ns, (iii) quenching to 298 K, (iv) simulating in NPT for 5 ns, followed with a subsequent production run of 100 ns at 298 K and 1 bar. The temperature of the system is controlled using a Nosé−Hoover thermostat while the pressure is controlled using a Parrinello-Rahman barostat. The electrostatic interactions are described with the Particle Mesh Ewald (PME) method[55] and the cut-off threshold of 12 Å is applied for both Coulomb and non-bonded Van der Waals interaction. The periodic boundary conditions (PBC) and LINCS algorithm are turned on during the production run.[56] Radial distribution function (RDF) and spatial distribution function (SDF) analyses are conducted based on the last 20 ns simulation trajectories.

3. RESULTS AND DISCUSSION

3.1 Thermodynamic and physical property-based screening

From the three chemical suppliers mentioned above, 170 commercially available and price-reasonable ILs are collected (as tabulated in Supporting Information Table S1), which can be paired with each other to generate practically accessible DSILs for the subsequent screening and validation steps. Based on this initial pool of 170 ILs, an enormous number of DSILs could be obtained if different molar ratios of parent ILs are accounted, offering a giant space for tuning DSIL properties. However, for the sake of

computational cost, only the molar ratio of 1:1 is considered for pairing parent ILs in the thermodynamic and physical property based DSIL screening, which results in 14,365 (C_{170}^2) DSIL candidates. The C^∞ and S^∞ of these 14,365 DSILs are calculated by the COSMO-RS model, while the T_m and η of the 170 parent ILs are collected from ILThermo or predicted by the deep learning method for physical property estimation of DSILs (detailed in Table S2, Supporting Information).

As shown in Figure 2a, the C^∞ and S^∞ of these DSILs have a much broader distribution as opposed to those of the 170 parent ILs, which are almost overcovered in this plot. This C^∞-S^∞ distribution directly demonstrates that DSILs provide more opportunities to achieve desirable thermodynamic properties. By further applying the constraints on T_m and η, a majority of these DSILs are discarded. However, if taking the same criteria on the ILs, the number of retaining DSILs is still much larger than that of retaining ILs (975 versus 20, as tabulated in Supporting Information Tables S3 and S4), as compared in Figure 2b. The broader C^∞-S^∞ distribution of DSILs in Figure 2b again indicates the wider thermodynamic property tunable range.

To further screen DSILs with competitive extraction power, sulfolane is employed as a benchmark because it is widely considered to be an efficient conventional solvent in dearomatization. Correspondingly, 77 of the 965 DSILs are preserved with higher C^∞ and S^∞ than those of sulfolane (C^∞=0.297, S^∞=10.620), whereas only three ILs are retained by imposing the same constraints (see Figure 3 with the detailed information tabulated in Tables S5 and S6). It is interesting to note that satisfying DSILs can even appear through the pairing of ILs discarded by the thermodynamic constraints. For example, $[C_{10}MIm]_{0.5}[C_2MIm]_{0.5}[NTf_2]$ is retained with higher C^∞ and S^∞ than sulfolane, while both its parent ILs namely $[C_{10}MIm][NTf_2]$ and $[C_2MIm][NTf_2]$ are eliminated by the thermodynamic property constraints. This finding well manifests the

advantages of DSILs in extending the solvent selection space and tuning the solvent properties. Among the 77 retained DSILs, five candidates can be connected to form a pseudo-Pareto front and no one below this front can surpass them in both C^{∞} and S^{∞}. For comparison, two of the three retained ILs can also be selected in a similar manner. Therefore, these five DSILs and two ILs will be validated by LLE experiments subsequently. The predicted C^{∞} and S^{∞} as well as the corresponding T_m and η of these selected DSILs and ILs are detailed in Table 1.

3.2 LLE experiments

Before experimental validation, the five DSILs screened above are prepared by mixing the corresponding IL parents. In all the five cases, a clear homogenous "mixture" is observed, demonstrating the viability for extraction. After obtaining the DSILs, the LLE experiments of {DSILs + *o*-xylene + *n*-octane} are performed at the same global composition, for which 2 g model mixture of *o*-xylene/*n*-octane (25 wt%/75 wt%) and 0.0047 mol (around 2 g) different DSILs are added into a screw-capped vial, respectively. Note that, a fixed mole rather than a fixed mass of DSIL is kept in the experiments to better compare with the molar-based C^{∞} and S^{∞} calculated by COSMO-RS. LLE experiments with the two screened referenced ILs are performed in the same manner. Figure 4 compares the experimentally-derived β and S of these five DSILs and two ILs (detailed in Table S7, Supporting Information), where the higher extractive power of DSILs can be generally validated as they form an exterior pseudo-Pareto front overcasting the ILs. This conclusion is much clearer if DSILs at different ion ratios are considered following the identical procedure, as illustrated with $[C_4MPyr]_x[C_4MMIm]_{1-x}[NTf_2]$ (x ranges from 0 to 1) as an example in Figure 4b. In this sense, these LLE results basically agree with the C^{∞}-S^{∞} trend predicted by COSMO-RS.

In tandem with $[C_4MPyr]_x[C_4MMIm]_{1-x}[NTf_2]$, $[C_4MMIm]_x[C_2MIm]_{1-x}[NTf_2]$ and

$[C_{10}MIm]_x[C_2MIm]_{1-x}[NTf_2]$ are selected as representatives to uncover the effect of different ion ratios on the extraction power of DSILs. As seen in Figures 5a and 5b, in the cases of $[C_4MMIm]_x[C_2MIm]_{1-x}$ and $[C_{10}MIm]_x[C_2MIm]_{1-x}$ $[NTf_2]$, the β gradually increases while the S gradually decreases with x changing from 0 to 1. Differently, as for $[C_4MPyr]_x[C_4MMIm]_{1-x}[NTf_2]$, a local maximum is observed at $x = 0.5$ for both β and S, despite of their general increasing and decreasing trends along the x-axis, respectively (see Figure 5c). That is to say, there may exist different dependencies of β and S on the ion ratios of DSIL systems (detailed in Table S8, Supporting Information). Nevertheless, these three cases all confirm that the ion ratios of DSILs have a significant effect on their thermodynamic properties, thus providing an elegant degree of freedom for tuning solvent properties.

3.3 Mechanism exploration

To better understand the mechanism for tuning DSIL properties toward extraction, theoretical calculations at the microscopic scale are performed as follows: (1) intermolecular interaction energy and IGM analyses based on quantum chemistry calculation; (2) RDF and SDF analyses based on molecular dynamics simulation. The DSIL system of $[C_4MPyr]_x[C_4MMIm]_{1-x}[NTf_2]$ is taken as a representative because it not only shares a similar general trend of β and S as the other two systems (i.e., $[C_4MMIm]_x[C_2MIm]_{1-x}[NTf_2]$ and $[C_{10}MIm]_x[C_2MIm]_{1-x}[NTf_2]$) with the variation of ion ratios but also experiences an interesting local maximum of β and S at $x = 0.5$.

On the basis of DFT calculation, the most stable geometric structures of the parent ILs (i.e., $[C_4MPyr][NTf_2]$ and $[C_4MMIm][NTf_2]$) as well as *n*-octane and *o*-xylene are used to analyze intermolecular interaction. Subsequently, the optimized structures and E_{inter} (detailed in Figure S1 and Table S9, Supporting Information) of (a) {$[C_4MPyr][NTf_2]$ + *n*-octane}, (b) {$[C_4MPyr][NTf_2]$ + *o*-xylene}, (c)

{[C_4MMIm][NTf_2] + *n*-octane}, (d) {[C_4MMIm][NTf_2] + *o*-xylene} are obtained to serve as the reference for the DSILs-involved systems. As shown in Figure 6, both parent ILs exhibit a notably stronger E_{inter} with *o*-xylene than with *n*-octane, indicating that they are both able to selectively extract the former from the latter. Moreover, the interaction of {[C_4MPyr][NTf_2] + *o*-xylene} is stronger than that of the {[C_4MMIm][NTf_2] + *o*-xylene} while the difference between {IL+ *o*-xylene} and {IL + *n*-octane} interactions (ΔE) is larger in the case of [C_4MMIm][NTf_2], which can jointly explain the higher β and lower S of [C_4MPyr][NTf_2] for this extraction system. Based on such IL-solute interaction energy analysis, a higher molar ratio of [C_4MPyr][NTf_2] in [C_4MPyr]$_x$[C_4MMIm]$_{1-x}$[NTf_2] would potentially increase the β but decrease the S, which is consistent with the general trends of β and S identified by LLE experiments.

To further identify the type of intermolecular interactions in different solvent-solute systems, color-filled IGM maps for the {[C_4MPyr][NTf_2]/[C_4MMIm][NTf_2]/ [C_4MPyr]$_{0.5}$[C_4MMIm]$_{0.5}$[NTf_2] + *n*-octane/*o*-xylene} are obtained and visually presented in Figure 7. As seen, there are merely green thin isosurfaces between solvent and solute in all these cases, indicating that both the two parent ILs as well as the DSIL interact with the solutes (i.e., *n*-octane and *o*-xylene) mainly by van der Waals (vdW) interactions.

In addition to the above quantum chemistry calculation, molecular dynamics simulations are further performed for the systems of {[C_4MPyr]$_x$[C_4MMIm]$_{1-x}$[NTf_2] + *o*-xylene + *n*-octane} (x = 0.2, 0.4, 0.5, 0.6, 0.8) for interaction analysis and for investigating the effect of different ion ratios in the DSIL-involved systems directly. Figure 8 illustrates the organization of cations and anions around *o*-xylene as a function of the [C_4MPyr]$^+$ concentration through spatial distribution functions (SDFs) at 298 K.

As opposed to the anion, both the two cations possess larger and closer isosurface density region around *o*-xylene, indicating that the interactions between DSIL and *o*-xylene are dominated by the cations. Moreover, the cations are mainly dispersed in parallel to the plane of aromatic ring, which suggests the formation of CH-π or π-π interactions. As for the two cations, a much larger area of $[C_4MPyr]^+$ isosurface appearing at the parallel plane of the aromatic ring can be observed than that of $[C_4MMIm]^+$, which manifests a stronger {$[C_4MPyr]^+$ + *o*-xylene} interaction than the {$[C_4MMIm]^+$ + *o*-xylene} interaction. This finding is in line with the conclusion drawn from the E_{inter} analysis, where $[C_4MPyr][NTf_2]$ presents a higher E_{inter} with *o*-xylene in comparison to $[C_4MMIm][NTf_2]$.

The RDFs of {$[C_4MPyr]^+$/$[C_4MMIm]^+$ + *n*-octane/*o*-xylene} are illustrated in Figure 9. Due to the positive correlation between the first peak intensity and intermolecular interaction strength, the peak intensity of g(r) in Figures 9a and 9c again indicates a stronger {$[C_4MPyr]^+$ + *n*-octane} interaction than the {$[C_4MMIm]^+$ + *n*-octane} interaction. Similarly, the stronger interaction of{$[C_4MPyr]^+$ + *o*-xylene} than that of {$[C_4MMIm]^+$ + *o*-xylene} could be demonstrated from Figures 9b and 9d. As shown in Figures 9a and 9b, with *x* of 0.2, 0.4, 0.6, and 0.8, the intensities of the first peak successively increase with the higher mole fraction of $[C_4MPyr]^+$. Interestingly, when *x* equals to 0.5 (i.e., $[C_4MPyr]_{0.5}[C_4MMIm]_{0.5}[NTf_2]$), a higher first peak of {$[C_4MPyr]^+$ + *o*-xylene} RDF compared to those in $[C_4MPyr]_{0.6}[C_4MMIm]_{0.4}[NTf_2]$-involved systems is observed whereas the first peak of {$[C_4MPyr]^+$ + *n*-octane} RDF is almost overlapped with the $[C_4MPyr]_{0.4}[C_4MMIm]_{0.6}[NTf_2]$-involved systems. That is to say, the {$[C_4MPyr]^+$ + *o*-xylene} and {$[C_4MPyr]^+$ + *o*-xylene/*n*-octane} interaction would likely to be enhanced as increasing the mole fraction of $[C_4MPyr]^+$, with a local exception at $x = 0.5$. Such RDF results well address the ion ratio-dependencies of β and

S of $[C_4MPyr]_x[C_4MMIm]_{1-x}[NTf_2]$ for the *o*-xylene/*n*-octane extraction.

4. CONCLUSION

A systematic framework combining the rational screening-validation and deep mechanistic exploration is first proposed and applied to investigate DSILs as extraction solvents for enhancing the *o*-xylene/*n*-octane separation. Among 14,365 DSILs paired from 170 commercially available ILs, five DSILs are screened as promising candidate solvents, showing higher extractive potential than the as-screened reference ILs and conventional solvent. The experimental LLE of {DSIL + *o*-xylene + *n*-octane} demonstrate the high extraction power of these DSILs and thus validate the reliability of the screening process. Moreover, the significant effect of ion ratio on the extraction power of DSILs is also uncovered by LLE experiments, proving it as an elegant degree of freedom for tuning the properties of DSILs. The interaction energies and IGM analyses based on quantum chemistry calculation, along with the SDF and RDF analyses based on molecular dynamics simulation, jointly elucidate that: (1) the extraction of *o*-xylene from *n*-octane is mainly dominated by the stronger vdW interactions with cations (in terms of CH-π or π-π interaction); (2) with varying *x*, the {DSIL+ solute} interactions are likely to change monotonously in the range of the {parent IL + solute} interactions while the variation trend may exist local exceptions (leading to non-monotonic behaviors of macroscopic properties, e.g., β and *S* in extraction). As DSILs open new avenues for designing IL-type solvents, the proposed framework in this work could be readily adapted to guide the rational selection and wide application of practical DSILs toward other separation systems.

ACKNOWLEDGEMENTS

This research is supported by the National Natural Science Foundation of China (NSFC) under the grants of 22208098, 22278134, and 21CAA01709.

DATA AVAILABILITY AND REPRODUCIBILITY STATEMENT

The numerical data from Figures 2-5 are tabulated in the Supplementary Material (Tables S1-S8). For quantum chemistry calculation, the detailed data for interaction energies between each parent IL and *o*-xylene/*n*-octane are available as Table S9 in the Supplementary Material. The compilation of input files from molecular dynamics simulation are also available as a .zip file in the Supplementary Material. These input files include complete information on the force fields and other simulation settings that were used in our GROMACS calculations.

REFERENCES

1. Tsai C, McNeeley A, Lin S, Liu YA. Evaluation of thermophysical data, COSMO-SAC predictions, and feed simplifications for aromatic extraction process simulation using ionic liquid [EMIM][NTf_2]. *AIChE J*. 2023;69(2):e17916.
2. Ashour I, Abu-Eishah SI. Liquid−liquid equilibria for cyclohexane + ethylbenzene + sulfolane at (303.15, 313.15, and 323.15) K. *J Chem Eng Data*. 2006;51(3):859-863.
3. Alkhaldi KHAE, Fandary MS, Al-Jimaz AS, Al-Tuwaim MS, Fahim MA. Liquid–liquid equilibria of aromatics removal from middle distillate using NMP. *Fluid Phase Equilibria*. 2009;286(2):190-195.
4. Li G, Gao Q, Liu Q, Gui C, Lei Z. Extraction of polycyclic aromatic hydrocarbons from fluid catalytic cracking diesel with ionic liquids. *AIChE J*. 2023;69(2):e17914.
5. Dai Z, Ansaloni L, Gin DL, Noble RD, Deng L. Facile fabrication of CO_2 separation membranes by cross-linking of poly(ethylene glycol) diglycidyl ether with a diamine and a polyamine-based ionic liquid. *J Membr Sci*. 2017;523:551-560.
6. Zheng S, Zeng S, Li Y, et al. State of the art of ionic liquid-modified adsorbents for CO_2 capture and separation. *AIChE J*. 2022;68(2):e17500.
7. Yang B, Bai L, Li T, et al. Super selective ammonia separation through multiple-site interaction with ionic liquid-based hybrid membranes. *J Membr Sci*. 2021;628:119264.
8. McNeeley A, Tsai C, Lin S, Liu YA. Development of energy-optimum aromatic extraction processes using ionic liquid [EMIM][NTf_2]. *AIChE J*. 2023;69(2): e17888.
9. Dai Z, Ansaloni L, Ryan JJ, Spontak RJ, Deng L. Nafion/IL hybrid membranes with

tuned nanostructure for enhanced CO_2 separation: effects of ionic liquid and water vapor. *Green Chem*. 2018;20(6):1391-1404.

10. Qin H, Xie K, Li L, Cheng J, Song Z. Enhancing R410A blend separation by using ionic liquids: from UNIFAC model extension, solvent design to molecular dynamics simulation. *Chem Eng Sci*. 2023;274:118709.
11. Yu G, Jin D, Li X, et al. Extractive desulfurization of model fuels with a nitrogen-containing heterocyclic ionic liquid. *Front Chem Sci Eng*. 2022;16(12):1735-1742.
12. You L, Guo Y, He Y, et al. Molecular level understanding of CO_2 capture in ionic liquid/polyimide composite membrane. *Front Chem Sci Eng*. 2022;16(2):141-151.
13. Song Z, Zhang C, Qi Z, Zhou T, Sundmacher K. Computer-aided design of ionic liquids as solvents for extractive desulfurization. *AIChE J*. 2018;64(3):1013-1025.
14. McNeeley A, Tsai C, Lin S, Liu YA. Science-guided data analytics for selecting ionic liquid solvents for aromatic extraction. *AIChE J*. 2023;69(6):e18081.
15. Zhao Y, Gani R, Afzal RM, Zhang X, Zhang S. Ionic liquids for absorption and separation of gases: an extensive database and a systematic screening method. *AIChE J*. 2017;63(4):1353-1367.
16. Sosa JE, Santiago R, Redondo AE, et al. Design of ionic liquids for fluorinated gas absorption: COSMO-RS selection and solubility experiments. *Environ Sci Technol*. 2022;56(9):5898-5909.
17. Song Z, Zhou T, Qi Z, Sundmacher K. Systematic method for screening ionic liquids as extraction solvents exemplified by an extractive desulfurization process. *ACS Sustain Chem Eng*. 2017;5(4):3382-3389.
18. Li G, Gui C, Zhu R, Lei Z. Deep eutectic solvents for efficient capture of cyclohexane in volatile organic compounds: thermodynamic and molecular mechanism. *AIChE J*. 2022;68(3):e17535.

19. Larriba M, Ayuso M, Navarro P, et al. Choline chloride-based deep eutectic solvents in the dearomatization of gasolines. *ACS Sustain Chem Eng*. 2018;6(1):1039-1047.
20. Ruan J, Ye X, Wang R, Chen L, Deng L, Qi Z. Experimental and theoretical study on efficient CO_2 absorption coordinated by molecules and ions of DBN and 1,2,4-triazole formed deep eutectic solvents. *Fuel*. 2023;334:126709.
21. Gui C, Li G, Song M, Lei Z. Absorption of dichloromethane in deep eutectic solvents: experimental and computational thermodynamics. *Sep Purif Technol*. 2023;311:123281.
22. Yu G, Gajardo-Parra NF, Chen M, Chen B, Sadowski G, Held C. Aromatic volatile organic compounds absorption with phenyl-based deep eutectic solvents: a molecular thermodynamics and dynamics study. *AIChE J*. 2023;69(5):e18053.
23. Sun L, Luo F, Liu R, Yang H, Huang L, Li J. Isobaric liquid–liquid equilibrium measurements and thermodynamics modeling for systems: benzene + cyclohexane + DESs at 303.15 and 323.15 K. *J Chem Eng Data*. 2019;64(3):1113-1121.
24. Cheng H, Liu C, Zhang J, Chen L, Zhang B, Qi Z. Screening deep eutectic solvents for extractive desulfurization of fuel based on COSMO-RS model. *Chem Eng Process - Process Intensif*. 2018;125:246-252.
25. Chen J, Zhu F, Qin H, Song Z, Qi Z, Sundmacher K. Rational eutectic solvent design by linking regular solution theory with QSAR modelling. *Chem Eng Sci*. 2022;262:118042.
26. Navarro P, Larriba M, García J, Rodríguez F. Design of the recovery section of the extracted aromatics in the separation of BTEX from naphtha feed to ethylene crackers using [4empy][Tf_2N] and [emim][DCA] mixed ionic liquids as solvent. *Sep Purif Technol*. 2017;180:149-156.
27. Larriba M, Navarro P, Delgado-Mellado N, González C, García J, Rodríguez F.

Dearomatization of pyrolysis gasoline with an ionic liquid mixture: experimental study and process simulation. *AIChE J*. 2017;63(9):4054-4065.

28. Lee BS, Lin ST. Prediction and screening of solubility of pharmaceuticals in single- and mixed-ionic liquids using COSMO-SAC model. *AIChE J*. 2017;63(7):3096-3104.
29. Song Z, Hu X, Zhou Y, Zhou T, Qi Z, Sundmacher K. Rational design of double salt ionic liquids as extraction solvents: separation of thiophene/*n* -octane as example. *AIChE J*. 2019;65(8):e16625.
30. Chatel G, Pereira JFB, Debbeti V, Wang H, Rogers RD. Mixing ionic liquids – "simple mixtures" or "double salts"? *Green Chem*. 2014;16(4):2051.
31. Lei Z, Han J, Zhang B, Li Q, Zhu J, Chen B. Solubility of CO_2 in binary mixtures of room-temperature ionic liquids at high pressures. *J Chem Eng Data*. 2012;57(8):2153-2159.
32. Chen G, Song Z, Qi Z, Sundmacher K. Generalizing property prediction of ionic liquids from limited labeled data: a one-stop framework empowered by transfer learning. *Digit Discov*. 2023;2(3):591-601.
33. Eckert F, Klamt A. Fast solvent screening via quantum chemistry: COSMO-RS approach. *AIChE J*. 2002;48(2):369-385.
34. Bedia J, Ruiz E, de Riva J, Ferro VR, Palomar J, Rodriguez JJ. Optimized ionic liquids for toluene absorption. *AIChE J*. 2013;59(5):1648-1656.
35. Moreno D, Ferro VR, De Riva J, et al. Absorption refrigeration cycles based on ionic liquids: refrigerant/absorbent selection by thermodynamic and process analysis. *Appl Energy*. 2018;213:179-194.
36. Yu G, Wei Z, Chen K, Guo R, Lei Z. Predictive molecular thermodynamic models for ionic liquids. *AIChE J*. 2022;68(4):e17575.

37. Qin H, Cheng J, Yu H, Zhou T, Song Z. Hierarchical ionic liquid screening integrating COSMO-RS and Aspen Plus for selective recovery of hydrofluorocarbons and hydrofluoroolefins from a refrigerant blend. *Ind Eng Chem Res*. 2022;61(11):4083-4094.

38. Potdar S, Anantharaj R, Banerjee T. Aromatic extraction using mixed ionic liquids: experiments and COSMO-RS predictions. *J Chem Eng Data*. 2012;57(4):1026-1035.

39. Fernandez L, Silva LP, Martins MAR, et al. Indirect assessment of the fusion properties of choline chloride from solid-liquid equilibria data. *Fluid Phase Equilibria*. 2017;448:9-14.

40. Stoppa A, Buchner R, Hefter G. How ideal are binary mixtures of room-temperature ionic liquids? *J Mol Liq*. 2010;153(1):46-51.

41. Larriba M, García S, Navarro P, García J, Rodríguez F. Physical characterization of an aromatic extraction solvent formed by [bpy][BF_4] and [4bmpy][Tf_2N] mixed ionic liquids. *J Chem Eng Data*. 2013;58(6):1496-1504.

42. Grunberg L, Nissan AH. Mixture law for viscosity. *Nature*. 1949;164(4175):799-800.

43. Chirico RD, Frenkel M, Diky VV, Marsh KN, Wilhoit RC. ThermoML-an XML-based approach for storage and exchange of experimental and critically evaluated thermophysical and thermochemical property data. 2. uncertainties. *J Chem Eng Data*. 2003;48(5):1344-1359.

44. Li Z, Dai C, Zhu J, Lei Z, Zhang J, Yu G. Thermodynamics and molecular insights into anionic structural effects on toluene absorption with ionic liquids. *Chem Eng Sci*. 2023;276:118817.

45. Han J, Fan Y, Yu G, et al. Ethanol dehydration with ionic liquids from molecular

insights to process intensification. *ACS Sustain Chem Eng*. 2022;10(1):441-455.

46. Zhao Y, Truhlar DG. Density functionals with broad applicability in chemistry. *Acc Chem Res*. 2008;41(2):157-167.
47. Grimme S, Ehrlich S, Goerigk L. Effect of the damping function in dispersion corrected density functional theory. *J Comput Chem*. 2011;32(7):1456-1465.
48. Van Duijneveldt FB, Van Duijneveldt-van De Rijdt JGCM, Van Lenthe JH. State of the art in counterpoise theory. *Chem Rev*. 1994;94(7):1873-1885.
49. Lefebvre C, Rubez G, Khartabil H, Boisson JC, Contreras-García J, Hénon E. Accurately extracting the signature of intermolecular interactions present in the NCI plot of the reduced density gradient versus electron density. *Phys Chem Chem Phys*. 2017;19(27):17928-17936.
50. Lu T, Chen F. Multiwfn: A multifunctional wavefunction analyzer. *J Comput Chem*. 2012;33(5):580-592.
51. Humphrey W, Dalke A, Schulten K. VMD: visual molecular dynamics. *J Mol Graph*. 1996;14(1):33-38.
52. Van Der Spoel D, Lindahl E, Hess B, Groenhof G, Mark AE, Berendsen HJC. GROMACS: fast, flexible, and free. *J Comput Chem*. 2005;26(16):1701-1718.
53. Zhang J, Lu T. Efficient evaluation of electrostatic potential with computerized optimized code. *Phys Chem Chem Phys*. 2021;23(36):20323-20328.
54. Wang J, Wolf RM, Caldwell JW, Kollman PA, Case DA. Development and testing of a general amber force field. *J Comput Chem*. 2004;25(9):1157-1174.
55. Essmann U, Perera L, Berkowitz ML, Darden T, Lee H, Pedersen LG. A smooth particle mesh Ewald method. *J Chem Phys*. 1995;103(19):8577-8593.
56. Ryckaert JP, Ciccotti G, Berendsen HJC. Numerical integration of the cartesian equations of motion of a system with constraints: molecular dynamics of *n*-alkanes.

J Comput Phys. 1977;23(3):327-341.

SUPPORTING INFORMATION

Additional supporting information can be found online in the Supporting Information section at the end of this article.

Table 1. Selected DSILs and ILs for experimental validation after thermodynamic and physical property-based screening.

Solvents	C^{∞}	S^{∞}	T_m/K (parent 1/2)	η/mPa·s
$[C_4MMIm]_{0.5}[C_2MIm]_{0.5}[NTf_2]$	0.328	17.999	341.79*/266.40	58.65
$[C_4MMIm]_{0.5}[C_3MIm]_{0.5}[NTf_2]$	0.375	15.711	341.79*/260.64*	63.01
$[C_4MMIm]_{0.5}[C_4MIm]_{0.5}[NTf_2]$	0.417	14.137	341.79*/271.10	71.27
$[C_4MPyr]_{0.5}[C_4MMIm]_{0.5}[NTf_2]$	0.457	12.533	261.20/341.79*	88.60
$[C_{10}MIm]_{0.5}[C_2MIm]_{0.5}[NTf_2]$	0.502	11.356	276.20*/266.40	58.91
$[C_4MIm][NTf_2]$	0.353	15.971	271.10	50.80
$[C_4MPyr][NTf_2]$	0.429	12.273	261.20	78.50

*Note**:** properties predicted by the deep learning model.

Figure captions

Figure 1. Research framework proposed in this work.

Figure 2. COSMO-RS predicted infinite dilution capacity (C^{∞}) and selectivity (S^{∞}) of: (a) all 14,365 DSILs and 170 ILs; (b) DSILs and ILs meeting T_m and η constraints.

Figure 3. Further screened ILs and DSILs by applying the C^{∞} and S^{∞} constraints with sulfolane as the benchmark, highlighting the ones selected for experiments.

Figure 4. Experimentally determined distribution coefficient (β) and selectivity (S) of the selected DSILs and ILs.

Figure 5. Experimentally determined β and S of (a) $[C_4MMIm]_x[C_2MIm]_{1-x}[NTf_2]$, (b) $[C_{10}MIm]_x[C_2MIm]_{1-x}[NTf_2]$, (c) $[C_4MPyr]_x[C_4MMIm]_{1-x}[NTf_2]$ as the function of x.

Figure 6. Interaction energies between each parent IL and o-xylene/n-octane.

Figure 7. Color-filled independent gradient model (IGM) maps for different solvent-solute systems. (a) {$[C_4MPyr][NTf_2]$ + *n*-octane}; (b) {$[C_4MPyr][NTf_2]$ + *o*-xylene}; (c) {$[C_4MMIm][NTf_2]$ + *n*-octane}; (d) {$[C_4MMIm][NTf_2]$ + *o*-xylene}; (e) {$[C_4MPyr]_{0.5}[C_4MMIm]_{0.5}[NTf_2]$ + *n*-octane}; (f) {$[C_4MPyr]_{0.5}[C_4MMIm]_{0.5}[NTf_2]$ + *o*-xylene}.

Figure 8. Isosurfaces of the center of mass of $[C_4MPyr]^+$ (Blue), $[C_4MMIm]^+$ (Red), and $[NTf_2]^-$ (Green) surrounding *o*-xylene in $[C_4MPyr]_x[C_4MMIm]_{1-x}[NTf_2]$-involved systems. (a) x = 0.2; (b) x = 0.4; (c) x = 0.5; (d) x = 0.6; (e) x = 0.8. Isosurface density is 2.5 times the bulk density.

Figure 9. RDFs of the center of mass of two cations around the center of mass of *n*-octane/*o*-xylene as the function of x in $[C_4MPyr]_x[C_4MMIm]_{1-x}[NTf_2]$. (a) {$[C_4MPyr]^+$ + *n*-octane}; (b) {$[C_4MPyr]^+$ + *o*-xylene}; (c) {$[C_4MMIm]^+$ + *n*-octane}; (d) {$[C_4MMIm]^+$ + *o*-xylene}.

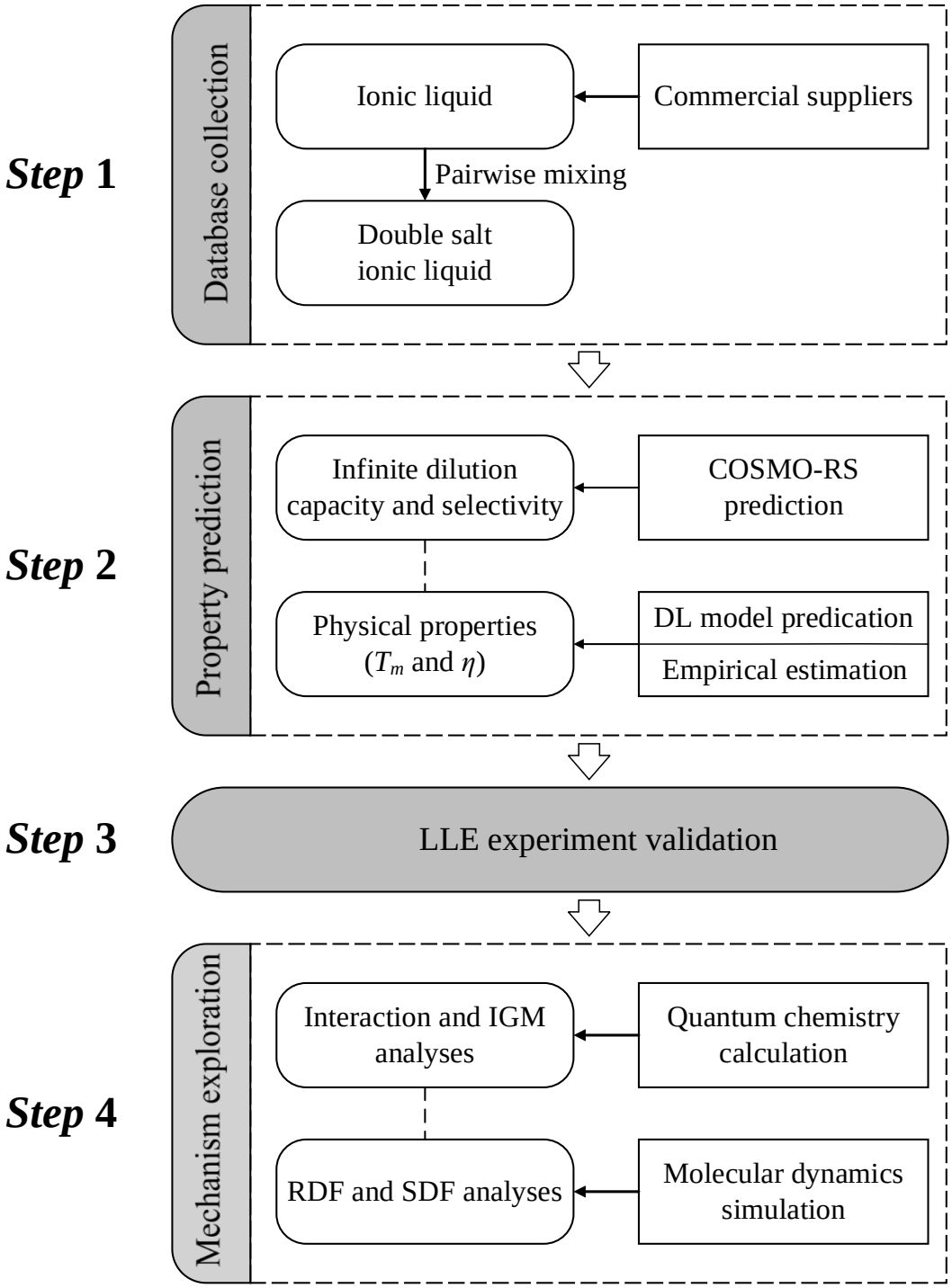

Figure 1. Research framework proposed in this work.

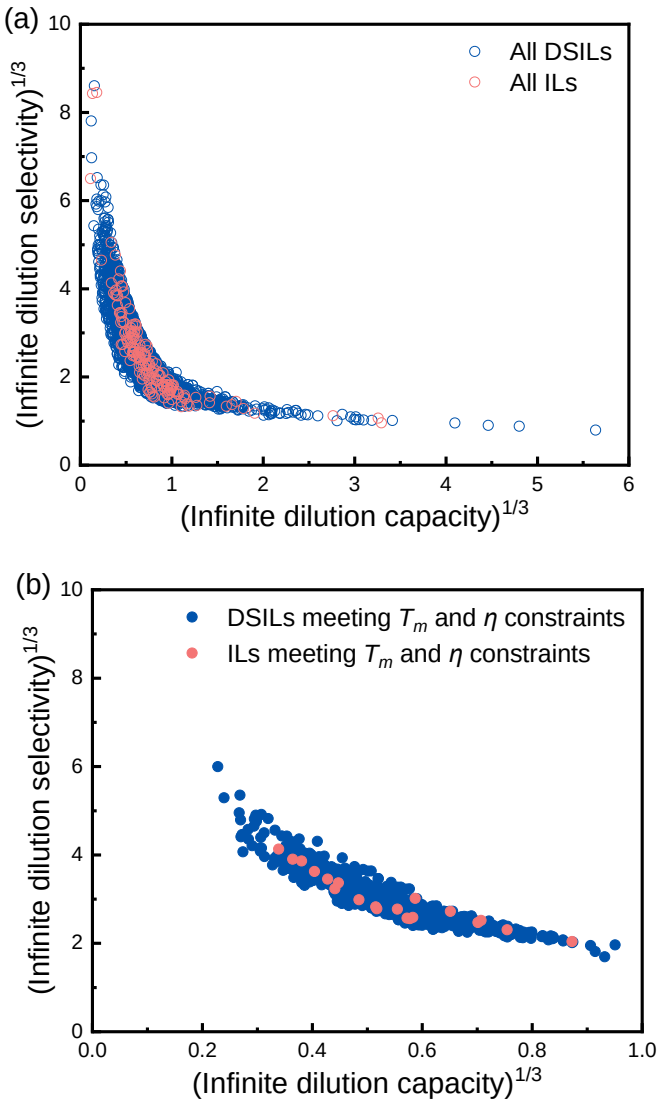

Figure 2. COSMO-RS predicted infinite dilution capacity (C^{∞}) and selectivity (S^{∞}) of: (a) all 14,365 DSILs and 170 ILs; (b) DSILs and ILs meeting T_m and η constraints.

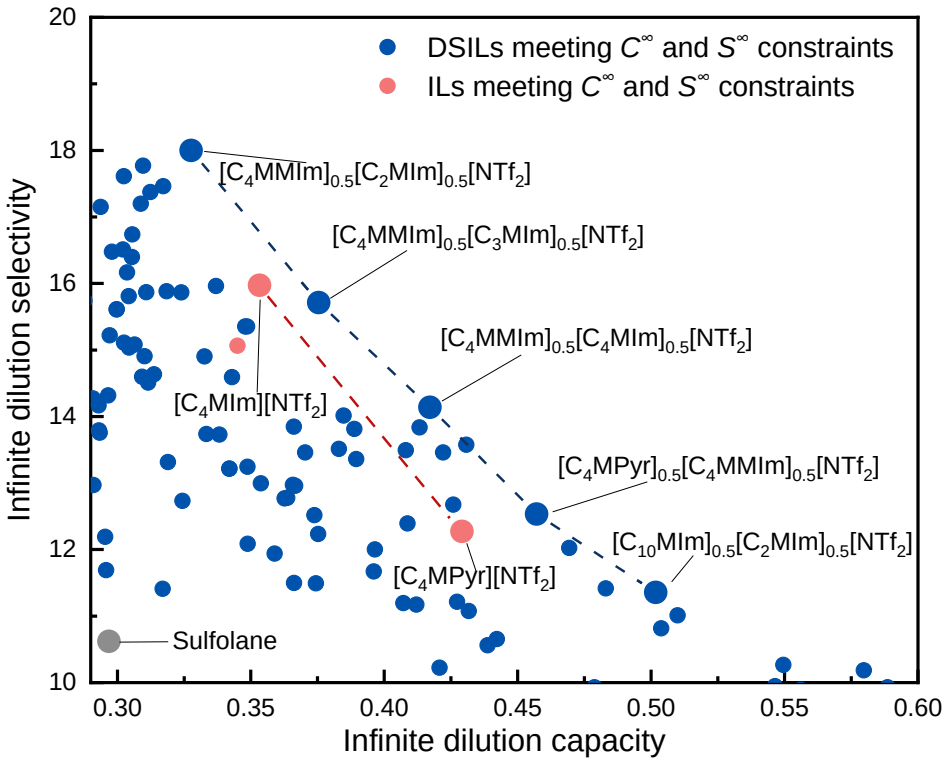

Figure3. Further screened ILs and DSILs by applying the C^{∞} and S^{∞} constraints with sulfolane as the benchmark, highlighting the ones selected for experiments.

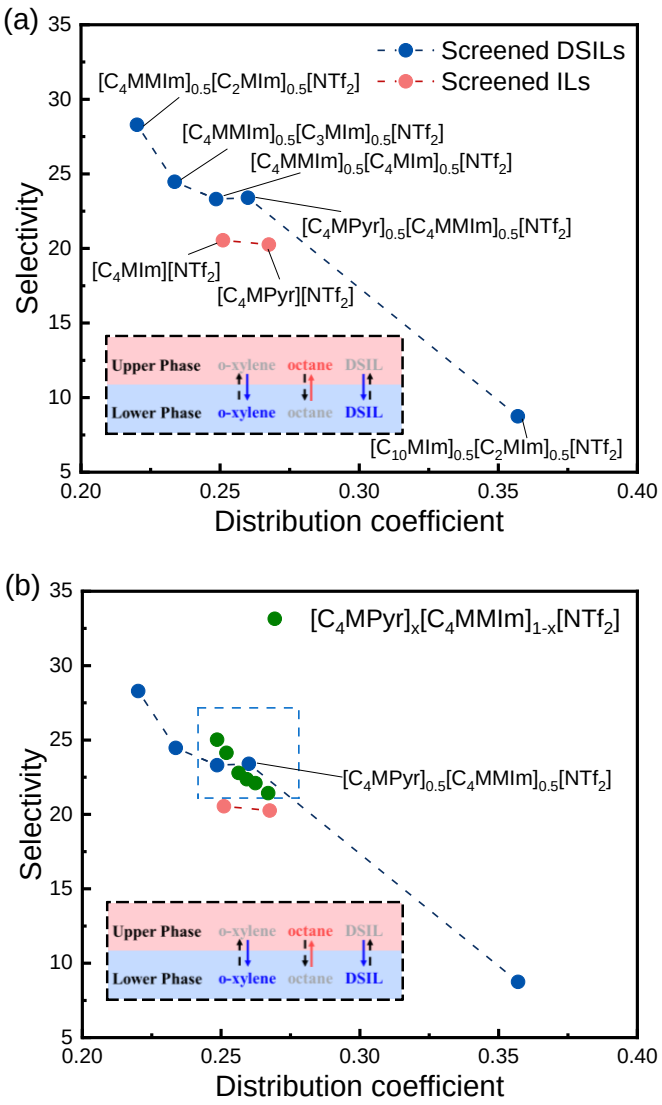

Figure 4. Experimentally determined distribution coefficient (β) and selectivity (S) of the selected DSILs and ILs.

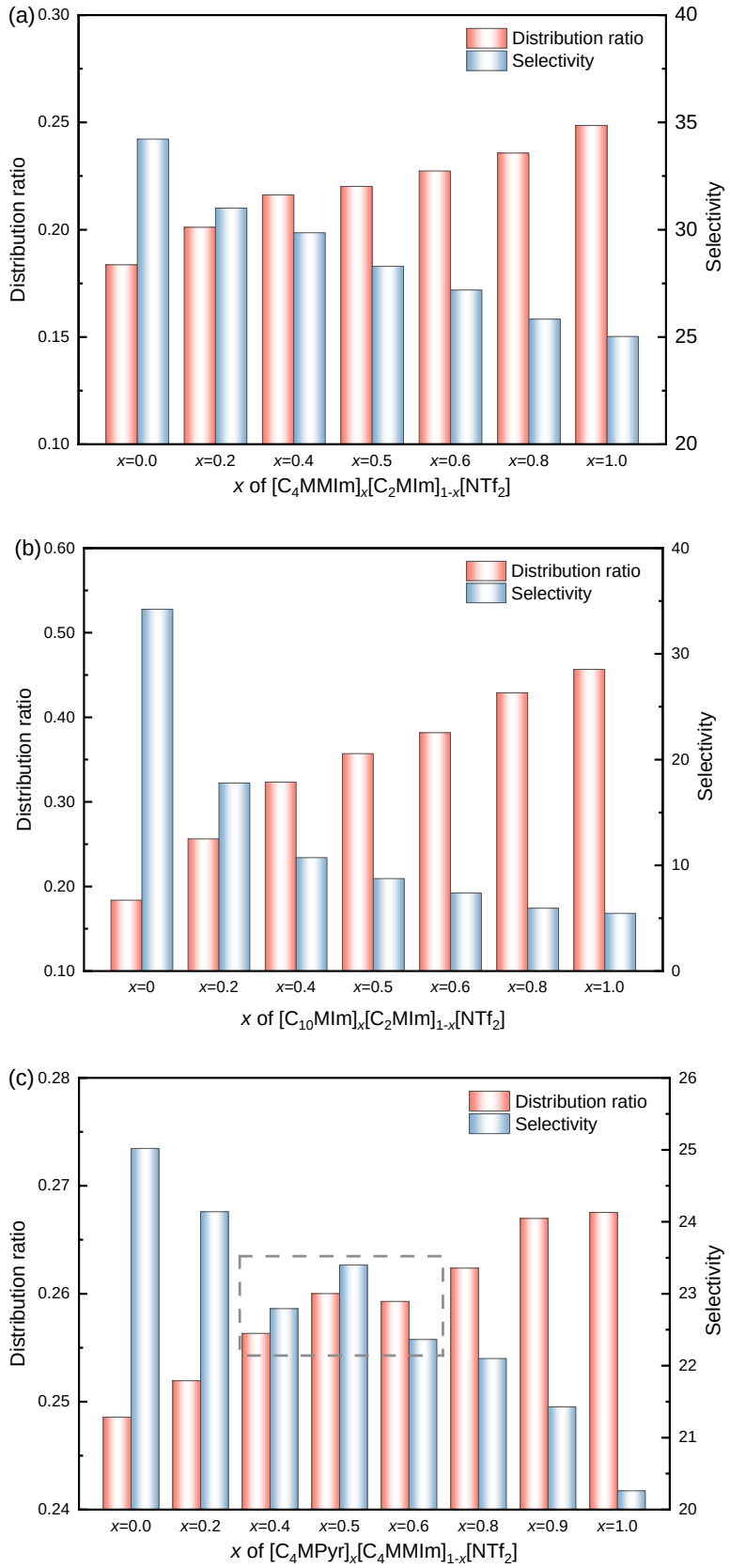

Figure 5. Experimentally determined β and S of (a) $[C_4MMIm]_x[C_2MIm]_{1-x}[NTf_2]$, (b) $[C_{10}MIm]_x[C_2MIm]_{1-x}[NTf_2]$, (c) $[C_4MPyr]_x[C_4MMIm]_{1-x}[NTf_2]$ as the function of x.

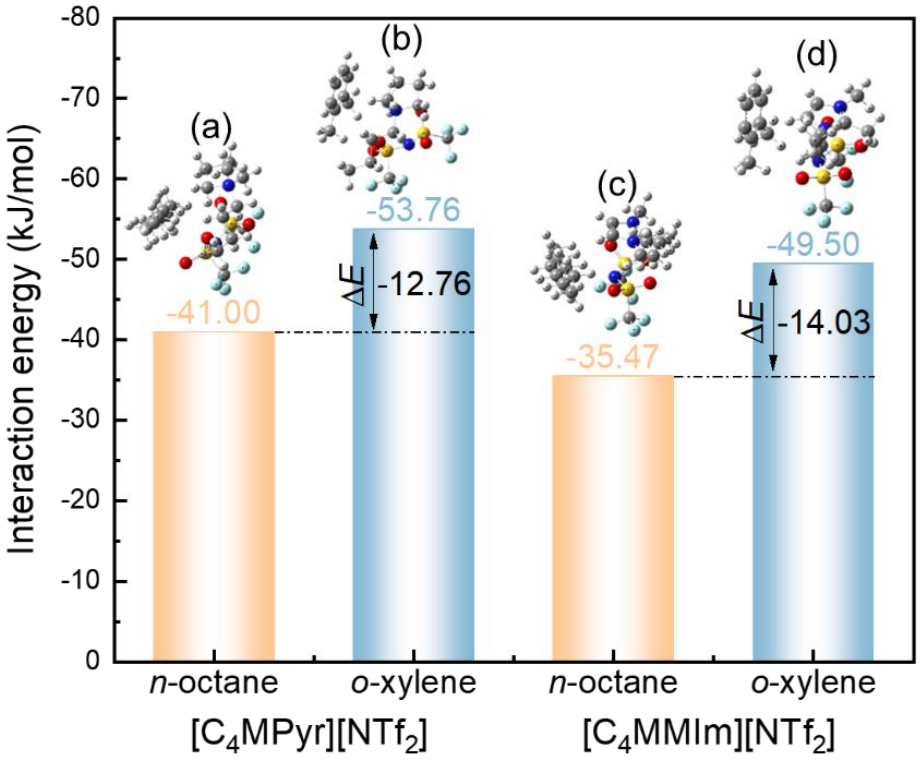

Figure 6. Interaction energies between each parent IL and *o*-xylene/*n*-octane (the original version of optimized geometric structures can be viewed in Figure S1).

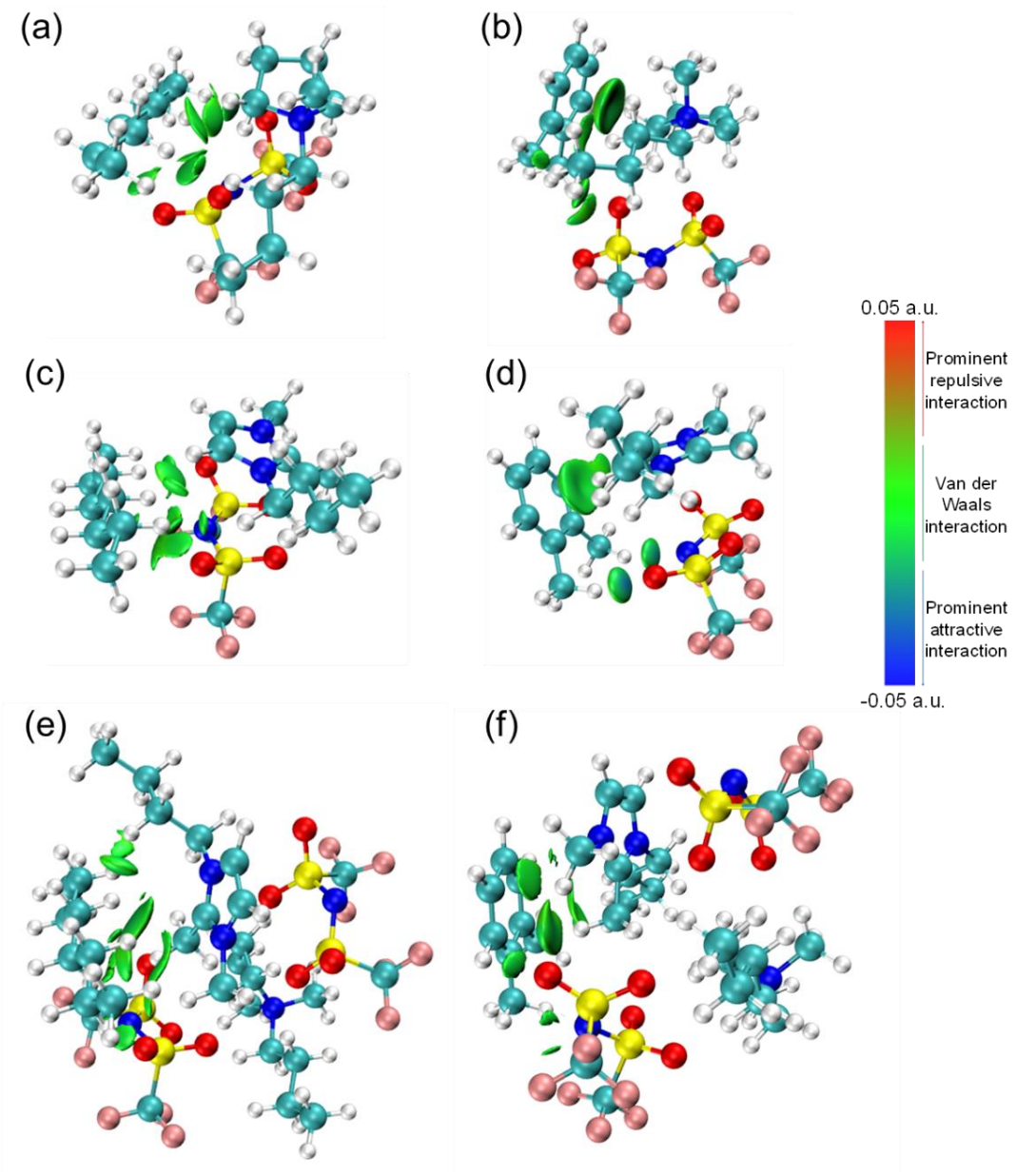

Figure 7. Color-filled independent gradient model (IGM) maps for different solvent-solute systems. (a) {[C_4MPyr][NTf_2] + *n*-octane}; (b) {[C_4MPyr][NTf_2] + *o*-xylene}; (c) {[C_4MMIm][NTf_2] + *n*-octane}; (d) {[C_4MMIm][NTf_2] + *o*-xylene}; (e) {[C_4MPyr]$_{0.5}$[C_4MMIm]$_{0.5}$[NTf_2] + *n*-octane}; (f) {[C_4MPyr]$_{0.5}$[C_4MMIm]$_{0.5}$[NTf_2] + *o*-xylene}.

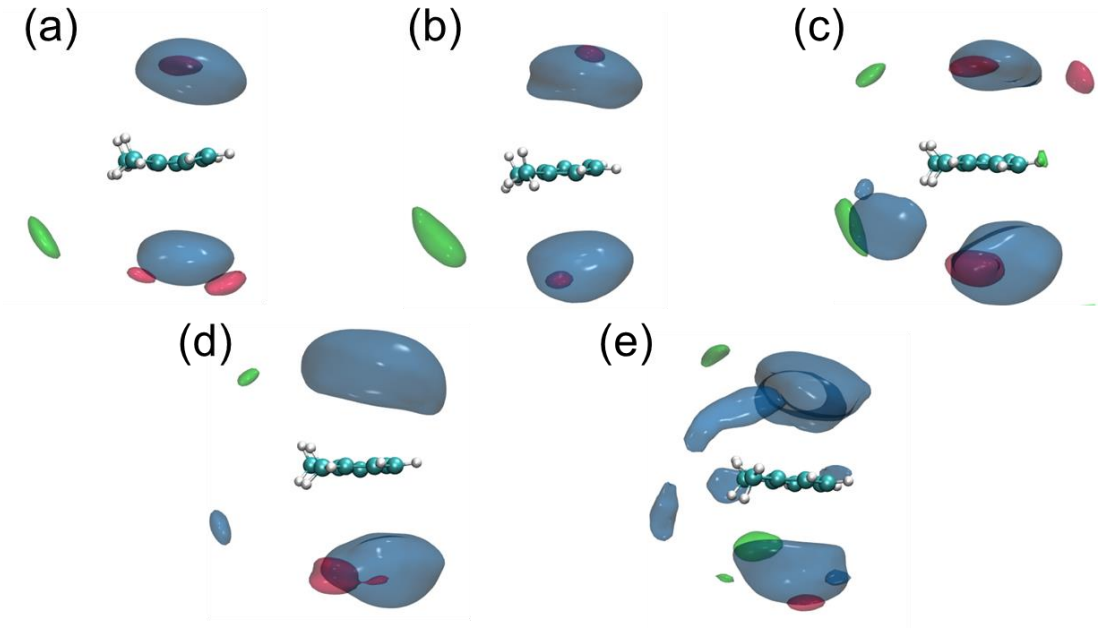

Figure 8. Isosurfaces of the center of mass of $[C_4MPyr]^+$ (Blue), $[C_4MMIm]^+$ (Red), and $[NTf_2]^-$ (Green) surrounding *o*-xylene in $[C_4MPyr]_x[C_4MMIm]_{1-x}[NTf_2]$-involved systems. (a) $x = 0.2$; (b) $x = 0.4$; (c) $x = 0.5$; (d) $x = 0.6$; (e) $x = 0.8$. Isosurface density is 2.5 times the bulk density.

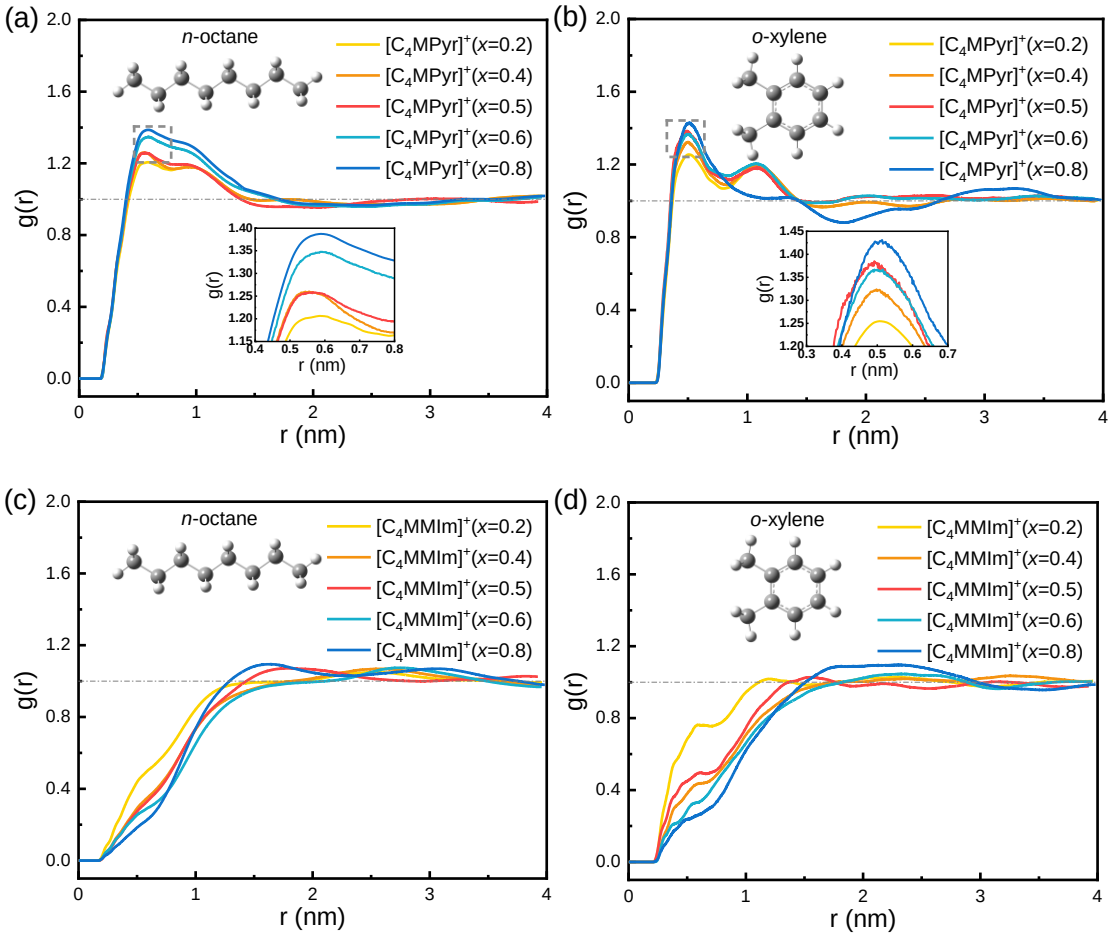

Figure 9. RDFs of the center of mass of two cations around the center of mass of *n*-octane/*o*-xylene as the function of *x* in $[C_4MPyr]_x[C_4MMIm]_{1-x}[NTf_2]$. (a) $\{[C_4MPyr]^+ + n\text{-octane}\}$; (b) $\{[C_4MPyr]^+ + o\text{-xylene}\}$; (c) $\{[C_4MMIm]^+ + n\text{-octane}\}$; (d) $\{[C_4MMIm]^+ + o\text{-xylene}\}$.